

## Article

# Modeling Large Wood Transport in Semi-Congested Regime with Multiple Entry Points

Elisabetta Persi <sup>1,\*</sup> , Sabrina Meninno <sup>2</sup>, Gabriella Petaccia <sup>1</sup> , Stefano Sibilla <sup>1</sup> and Aronne Armanini <sup>3</sup>

<sup>1</sup> Department of Civil Engineering and Architecture, University of Pavia, 27100 Pavia, Italy; gabriella.petaccia@unipv.it (G.P.); stefano.sibilla@unipv.it (S.S.)

<sup>2</sup> CIMA Research Foundation, 17100 Savona, Italy; sabrina.meninno@cimafoundation.org

<sup>3</sup> Department of Civil, Environmental and Mechanical Engineering, University of Trento, 38122 Trento, Italy; aronne.armanini@unitn.it

\* Correspondence: elisabetta.persi@unipv.it

**Abstract:** Wood transport during flood events can increase inundation risk and should be included in numerical models to estimate the associated residual risk. This paper presents the application of a fully Eulerian model that considers floating wood as a passive superficial pollutant through the adaptation of the advection–diffusion equation. A set of experiments is performed in a sinusoidal flume with a contraction to model semi-congested wood transport. The variation of the log release position replicates the possible variability of large wood entrainment during real events. The experiments are used to validate the numerical model, providing a comparison of the wood mass transport. Different release modes are also tested. The model predicts the position of the released logs and the overall transported mass, independently of the release position and modes, with an accuracy that varies along the flume length and across the flume axis. The analysis of the experimental and numerical transport velocity shows that modulation of the transport velocity is needed to ensure adequate model performances for semi-congested conditions.



**Citation:** Persi, E.; Meninno, S.; Petaccia, G.; Sibilla, S.; Armanini, A. Modeling Large Wood Transport in Semi-Congested Regime with Multiple Entry Points. *Water* **2022**, *14*, 421. <https://doi.org/10.3390/w14030421>

Academic Editor: Ichiro Kimura

Received: 15 October 2021

Accepted: 7 January 2022

Published: 29 January 2022

**Publisher's Note:** MDPI stays neutral with regard to jurisdictional claims in published maps and institutional affiliations.



**Copyright:** © 2022 by the authors. Licensee MDPI, Basel, Switzerland. This article is an open access article distributed under the terms and conditions of the Creative Commons Attribution (CC BY) license (<https://creativecommons.org/licenses/by/4.0/>).

**Keywords:** large wood; advection–diffusion; Eulerian model; semi-congested transport

## 1. Introduction

River engineers and flood modelers shall provide an adequate response to the natural phenomena that threaten citizens' safety along rivers. Flood risk mitigation measures rely on the prediction of the effects related to events with certain return periods but can be invalidated or weakened if unexpected factors arise, such as the transport of large amounts of wood debris during floods.

Large wood is usually uprooted by landslides, debris flows, or erosion [1] and can be transported through the river network [2], reaching the main stream and accumulating at bridge piers, dams, or other in-line structures. The obstruction of bridge spans reduces the bridge conveyance capacity and originates inundations that may reach levels expected for higher return period events [3,4]. Dams spillways and check dams are affected by large wood, too, with their efficiency being strongly limited due to wood accumulation [5,6]. Overall, the gathering of large wood at in-line structures increases the hydraulic risk and leads to possible structural failure due to the combination of water pressure and local scouring [7,8]. The occurrence of such events in the last decade highlights the need to update flood mitigation measures to cope also with the residual risk connected to large wood transport.

Apart from wood removal, which needs to be carefully considered, balancing hydraulic safety and ecological and geomorphological drawbacks [9], common countermeasures include fins, deflectors, capturing structures or retention basins [10]. Several laboratory investigations were carried out to provide details on the efficacy of these structures as well as to test new retention systems. Debris deflectors, groin-like structures, and

fins proved to be scarcely effective, but they avoid at least direct contact between the wood and the bridge pier, reducing local scouring [11,12]. Bottom sills built upstream of bridge piers appear a valuable alternative that promotes wood flowing instead of its retention, although further experiments are needed to confirm the power of this newly proposed approach [13]. Inclined or transversal racks were also tested. Their efficiency in retaining wood during floods was assessed with flume experiments conducted both without [14–16] and with sediment transport [17]. As the backwater rise is reduced for smaller rack angles with respect to the horizontal, an attempt to install horizontal rods was also performed [18], showing that the trapping efficiency is smaller than that of vertical racks and that it depends on the ratio between rod spacing and wood length. To reduce the backwater rise, a recent solution, tested in flume experiments [11], employs two vertical racks on the riversides inclined upstream. The retention efficiency depends mainly on the structure inclination with respect to the riversides. Racks or debris visors protecting dam spillways are tested in experimental campaigns [19] and are installed in existing dams, too, together with floating booms [6]. Finally, retention basins that profit on river morphology and create diversion channels or depositional areas that trap wood with the aid of vertical racks are promising systems employed along rivers [8] or upstream of dam basins [20]. They require a careful design based on the local river characteristics, both in terms of river flow and abundance of wood pieces.

Seeing the efforts of the scientific community to develop appropriate large wood countermeasures, a step forward to encourage and spread greater awareness on this issue could be made thanks to equally applicable numerical models. For this purpose, flood numerical models are being revised to tackle large wood transport. The coupling of a discrete element method with the 2D solution of the shallow water equation has proven to be a reliable tool to predict large wood transport both in flume and real-scale applications. Such models consider the transport of every single wooden element as a consequence of the velocity [21], or of the forces [22–24], exerted by the flow and can compute the displacement and rotation on the water surface of large wood, as well as the interaction and, in some cases, the accumulation at in-line structures and the consequent backwater effect [3].

The detailed description of the three-dimensional behavior of both the flow and of the large wood helps in improving the model's accuracy, particularly when dealing with the design of capturing structures [25]. Furthermore, flume experiments showed that the vertical velocity component plays a significant role in large wood accumulation even at single bridge piers [26], thus highlighting the need to include this aspect also in numerical modeling.

During flood events, a large number of wooden elements may be involved, including large and small wood debris, leaves, and other materials. This is the case of congested and semi-congested transport [27], characterized by a stronger interaction between wooden materials. The wood mass mainly floats on the water surface and is transported as a wood carpet, similar to that observed in the early-stage formation of wood barriers at check dams [28], so that the detailed behavior of a single wood piece does not need to be specifically modeled. Such an observation leads to a different perspective for numerical models, abandoning the deterministic approach, typical of Lagrangian models, in favor of an Eulerian approach that focuses on the transport of overall wooden mass. Following such an assumption, an Eulerian model was developed [29] and applied to a simple sinusoidal geometry [30]. By considering large wood as a floating pollutant, the model couples the diffusion equation with the shallow water equation to estimate the propagation of the wood mass. The fully Eulerian approach, both for the fluid and for the wood, may help in overcoming some difficulties related to the characterization of single log geometries and initial conditions. When the total amount of wood is considered, the only information needed is the total wood mass and its position to estimate its entrainment. The total mass can be derived through the wood budget techniques available, e.g., [31–33], considering the characteristics of the local basin and providing information about the volume of wood that is accountable for transport. Reducing the required data is significant for model users,

due to the possible complications in obtaining detailed information, such as wood piece dimensions, density, percentage of large or small wooden pieces, initial orientation.

Nonetheless, a fully Eulerian model presents some limitations that need to be carefully addressed regarding both the transport and the accumulation mechanism. Regarding accumulation, the arrest mechanism should be considered with care since it cannot be modeled directly on the physics of the phenomenon but is more likely to follow a probabilistic approach as highlighted by laboratory analysis for bridge [34], check dams [35], or dam accumulations [36].

However, at this stage, the main interest of the authors is in assessing transport capabilities. Since, in real events, wood mass can be entrained from multiple points, e.g., from either bank, and it adds to floating wood material entrained upstream, the proposed model should be capable of also simulating such behavior. For this reason, a series of flume experiments were carried out, with cylindrical logs released from different points in a flume cross-section. The sinusoidal shape of the flume and the presence of a narrowing increase the interactions among logs. Modeling such test cases can verify (i) the model's ability in dealing with multiple sources of wood mass and with different entry modes; (ii) the overall accuracy in modeling wood transport, especially at the narrowing.

## 2. Materials and Methods

### 2.1. Experimental Setup

The experimental investigation was carried out at the University of Trento in an S-shaped flume [29] with a gradual Venturi-like narrowing, placed at half of the channel length and within its straight part (Figure 1). The flume has a 2 m wide rectangular section, which reduces to 1 m in the narrowest cross-section. The convergent, constriction and divergent parts of the Venturi-like narrowing are 1 m long, while the entire flume develops for about 22 m.

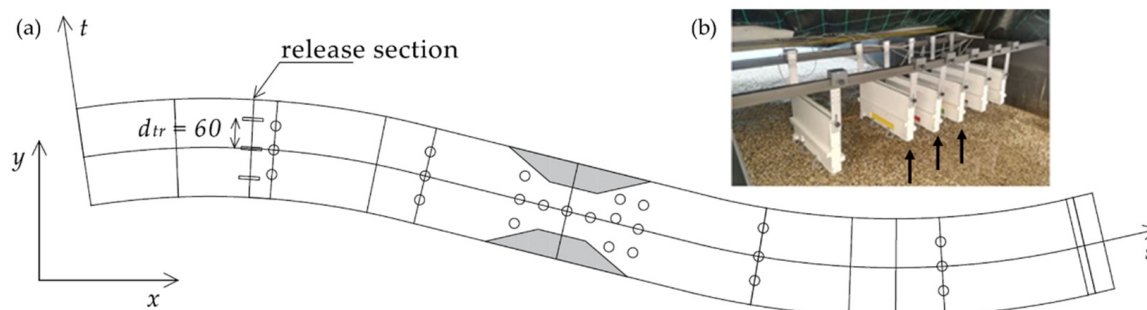


**Figure 1.** (a) Top view schematic of the flume, with the release distance set equal to  $d_{tr} = (-60, 0, 60)$  and (b) detail of the release boxes. Three black arrows show the boxes employed.

Hydraulic conditions were not varied during the campaign, with a discharge of 50 L/s, a slope of 0.43‰ over a fixed gravel bed ( $D_{50} = 8$  mm), and an average water level of 0.09 m. The Froude number was equal to 0.3 along the curves and 0.6 in the narrowing.

In the previous experimental campaign performed in the same flume, the logs were released one by one to avoid interactions, and the most probable positioning was analyzed [29]. In this case, the tests were performed by releasing simultaneously multiple wood pieces from three points on the same channel cross-section and in rapid succession to model a continuum mass of wood flowing through the flume. This test mode resembles a semi-congested transport regime, although maintaining a controlled approach to allow experiment replicability.

The release system is a mechanized device comprising three boxes mounted on a single support that is transverse to the channel. Each box has room for up to 10 wood pieces and is equipped with a motor that activates a hook pushing the wood into the water at regular intervals. The minimum time interval between two subsequent wood releases is 3 s, needed by the mechanism to work and to avoid cylinder overlapping.

The tests here presented employed three boxes at a variable distance of 20, 40, 60 cm from each other, placed respectively at  $d_{tr} = (-20, 0, 20)$ ,  $d_{tr} = (-40, 0, 40)$  and  $d_{tr} = (-60, 0, 60)$  with respect to the channel axes. Therefore, a single test comprised 30 wood pieces released every 3 s. Each test was repeated 5 times for statistical purposes.

Cylindrical logs, having a length  $L = 40$  cm and a diameter  $D = 2$  cm, were used to simulate real wood logs ( $L_r = 24$  m,  $D_r = 80$  cm), according to a distorted geometrical scale, described by a horizontal ratio  $\lambda_{xy} = 1/60$  and a vertical one of  $\lambda_z$  of  $1/40$ . Varnishing the logs helped to make them impermeable, keeping their density almost constant, of about  $790 \text{ km m}^{-3}$ , during the experimental campaign.

The wood pieces were filmed using three synchronized GoPro Hero 7 mounted at a height of 2.5 m on the channel, with a resolution of  $1920 \times 1080$  pixels, and by using 30 fps and a linear view.

To improve the tracing of the logs, several precautions were taken, such as the use of three colors to distinguish different adjacent wood pieces in the same image frame. Moreover, the combined use of a LED lighting system along the channel sidewalls and a cloth covering the entire flume was effective to minimize unwanted glares.

The tracking algorithm is similar to the one used in [29], with an improved filter to account for multiple logs in the same view, providing the trajectories of each log in terms of center coordinates and orientation.

## 2.2. Eulerian Numerical Model and Simulation Outlines

The numerical model ORSA2D, as modified in [30], is employed to model the transport of floating wood as a superficial pollutant. It is based on the one-way coupling of the shallow water equations and of the advection-diffusion equation for wood transport, which is derived from the continuity equation of the sole wood mass:

$$\frac{\partial \varphi}{\partial t} + \nabla \cdot \varphi \mathbf{v} = K_x \frac{\partial^2 \varphi}{\partial x^2} + K_y \frac{\partial^2 \varphi}{\partial y^2} \quad (1)$$

where  $\mathbf{v}(i, t) = (u, v)$  is the wood mass transport velocity and  $\varphi$  is volume averaged wood mass:

$$\varphi = \frac{c_w \rho_w}{h \, dx \, dy} \quad (2)$$

with  $c_w(x, t)$  being the probability of a wooden element occupying the position  $\mathbf{x} = (x, y)$  at time instant  $t$  times the wood volume inserted in the flume [ $\text{m}^3$ ], thus giving the volume fraction that can be found in a cell at a certain time. It gives the wood mass when multiplied by the wood density,  $\rho_w$ . The product  $h \, dx \, dy$  is the volume of water in the mesh cell,  $h$  is the water level. In Equation (1),  $K_x$  and  $K_y$  [ $\text{m}^2 \text{ s}^{-1}$ ] are the diffusion coefficients, computed from the streamwise and transversal values,  $K_s$  and  $K_t$  [29]:

$$K_s = 0.005 \, Fr_p^{-0.74} t_{Rr}^{-0.3} |\mathbf{v}(i, t)| L, \quad K_t = 0.011 \, Fr_p^{0.19} t_{Rr}^{0.27} |\mathbf{v}(i, t)| L; \quad (3)$$

where  $Fr_p$  is the particle Froude number, computed with the transport velocity at any cell  $i$  and time  $t$ , and log length  $L$  ( $Fr_p = |\mathbf{v}(i, t)| / \sqrt{gL}$ ) and  $t_{Rr}$  is the transversal relative release ( $t_{Rr} = \frac{t_R}{L}$ ) where  $t_R$  is the transversal distance between the right flume side and the right release point (80, 60 or 40 cm, for distance among boxes of 20, 40 and 60 cm, respectively). For the considered experimental conditions, the diffusion coefficients vary: (i) 0.016–0.022 times  $|\mathbf{v}(i, t)| L$  for the streamwise direction and (ii) 0.007–0.009 times  $|\mathbf{v}(i, t)| L$  for the transversal direction. The diffusion coefficient in the  $x$  and  $y$  directions are obtained by combining the streamwise and transversal values according to the velocity direction.

The wood mass transport velocity was modulated to replicate the inertia of the wood mass, based on experimental evidence of uncongested wood transport. The transport velocity depends on the flow velocity,  $\mathbf{v}_f(i, t)$ , the transversal release distance,  $t_R$ , and the

Froude number at the release position ( $Fr_{rel} = |v_f(i, t)| / \sqrt{gh(i)}$ , where  $h(i)$  is the local water level):

$$\begin{cases} v(i, t) = v_f(i, t) \left( 0.3 + 0.19 \left( 1 - e^{-\frac{t-t_0}{(4.39Fr_{rel})}} \right) \right) \frac{1.18}{0.49} & \text{if } v_f(i_{c \max}, t) - v_f(i_{c \max}, t - \Delta t) > \Delta v \\ v(i, t) = v_f(i, t) \left( 0.3 + 0.19 \left( 1 - e^{-\frac{t-t_0}{(4.39Fr_{rel})}} \right) \right) \frac{1.18}{0.49} (1 + 0.4t_R) & \text{if } v_f(i_{c \max}, t) - v_f(i_{c \max}, t - \Delta t) \leq \Delta v, \end{cases} \quad (4)$$

where  $t$  is the time and  $t_0$  is the initial time,  $i_{c \max}$  indicates the cell where the maximum concentration is found,  $\Delta t$  is the time step and  $\Delta v$  is an empirical threshold calibrated on uncongested transport experiments ( $\Delta v = -0.16$  m/s). Details of the mathematical derivation and on the transport velocity can be found in [30] (note that in the reference, the multiplication by fluid velocity is missing).

The original hydrodynamic model, without the advection–diffusion equation, was applied to several tests and real case simulations, being capable of dealing with different geometries and hydraulic conditions, from dam-break flooding [37] to 2D circulations in shallow lakes [38]. The coupled numerical model is solved with a finite-volume approach, implementing a Roe–Riemann scheme to solve the SWE. The details of the numerical model are the same described by Murillo et al. [39] in the coupling between SWE and solute flow. A correction of the numerical diffusion is also implemented [40]. The time step for the simulation is calculated considering the minimum time step between the one obtained with the Courant–Friedrich–Levy condition ( $CFL = 0.5$ ) and the one resulting from the Peclet number constraints.

The model is applied to the experimental tests described in Section 2.1.

The flume geometry is discretized by a mesh of about 19,600 triangular cells (average side 0.05 m) and a Manning coefficient of  $0.021 \text{ s m}^{-1/3}$ . The steady flow conditions are obtained by imposing a constant inflow upstream and constant Froude number as hydraulic outflow condition ( $Fr = 0.36$ , estimated during the experimental campaign through dedicated measurement at the end of the flume).

To simulate the flume experiments, 3 input points were defined by averaging the coordinates of the 10 logs released by each box (3 boxes for each test, 10 logs for each box) at the first frame they appeared in the recordings. This resulted in a triplet of coordinates that led to the identification of three input cells that slightly varied for each test and each repetition.

Unless wood entrainment is recorded by a passer or by a monitoring system, by chance, or for research purposes [2,41], the dynamic of large wood entrainment is generally unknown. Single logs can be entrained one by one (slow entrainment from the floodplain), or the whole wood volume may reach the stream resulting in an impulsive addition (wood uprooted by landslides or debris-flow).

In the experiment, only single entrainment from different points was tested to enhance the experiment's replicability. On the contrary, the various entrainment modes are simulated in the Eulerian model to assess their effect on wood transport dynamics. Figure 2 shows the input diagram of specific wood volume for one cell of area  $0.001246 \text{ m}^2$  (cell A, test 1, release distance 0.40 m, 10 cylinders). The wood volume is accounted for according to the following modes:

- *Single*: the mass of one log is released in 3 s; 10 logs are released for each box;
- *Continuum*: the mass of 10 logs is continuously released in a time interval of 27 s (10 logs released each 3 s, starting from  $t = 0$  s);
- *Cumulative*: the mass of 10 logs for each box is released in 3 s.

At the upstream boundary, a wood mass hydrograph is imposed in each input cell. The maximum specific release rate depends on the cell area and varies for each input point. For all the release modes, the total wood volume is obtained by the area under the curve in Figure 2a times the cell area. Figure 2b shows the location of the average mass center for test 1 with a release distance of  $-0.4$  cm. At the downstream boundary edge, the wood

mass concentration is computed according to a Neumann boundary condition by setting its derivative equal to zero [30].

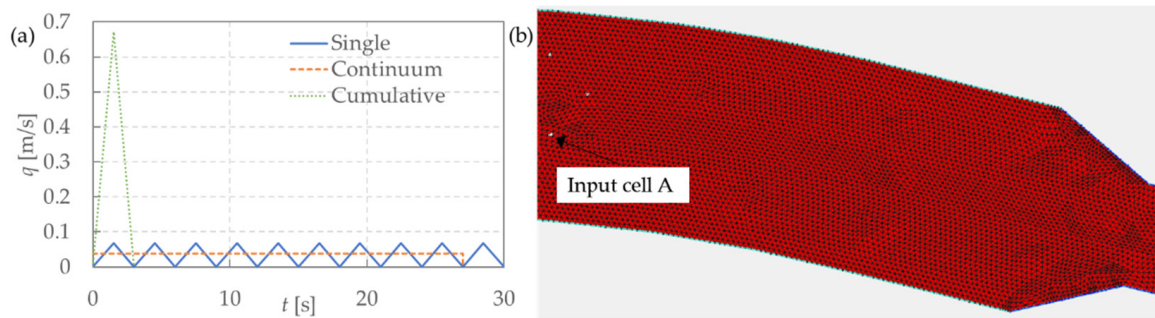


**Figure 2.** (a) Wood volume rate for the different release modes, (b) release cell positioning (both for a test with distance  $d_{tr} = (-40, 0, 40)$ , right cell).

### 3. Results

#### 3.1. Hydraulic Results and Wood Velocity Analysis

Figure 3 shows a comparison of the simulated water velocities, water levels, and water level profile at the flume axis with measured experimental values. The measurements were performed with a point gauge (water stage, difference between water level and local bottom elevation) and acoustic Doppler velocimeter (velocity measurements, ADV 2D Sontek). The comparison shows that the water profile along the axis is well represented, despite some inaccuracies in the constriction and the divergent ( $s = 11\text{--}13$  m). The correlation coefficient for Figure 3a is  $R^2 = 0.93$ , and the root mean square error is  $RMSE = 0.006$ . The maximum error, of about 1.7 cm, is observed at  $s = 12.12$ , where the simulation presents the minimum water level.

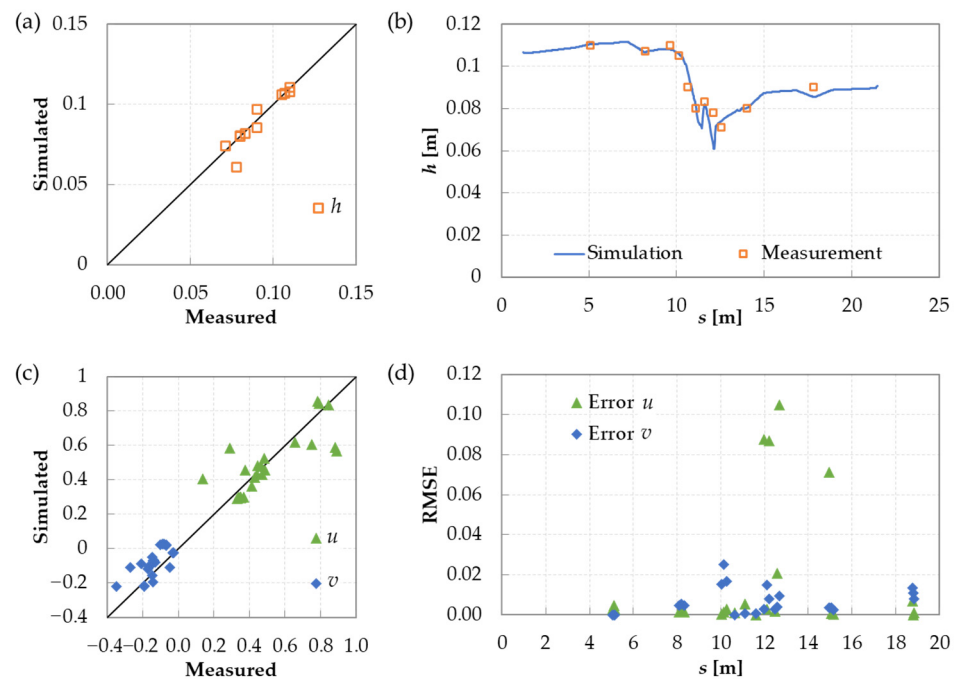


**Figure 3.** Comparison of the experimental and numerical hydraulic variables: (a) water level, (b) water level profile at flume axis, (c) water velocities; (d) root mean square error for the water velocity component along the flume.

Water velocities (Figure 3c,d) appear less accurate, with  $R^2 = 0.78\text{--}0.69$  and  $RMSE = 0.13\text{--}0.08$  for the velocity components  $u$  and  $v$  respectively. In particular, the Cartesian velocity plotted

along the  $s$  direction is more dispersed and presents the highest errors in the divergent and final reaches ( $s > 12$  m).

The observed differences between the measured and simulated flow velocities may affect wood transport even if the wood transport velocity in the simulation is the most significant parameter (Equation (4), hereafter indicated simply as transport velocity) and must be compared with the cylinder velocity observed in the experimental campaign.

Figure 4a shows the experimental velocity of the 30 wood pieces tracked during a single test with release distance  $d_{tr} = (-40, 0, 40)$  compared with the sampled average experimental velocity (see Section 3.3 for sampling details), the simulated flow velocity along the experimental average trajectory and an average transport velocity computed by applying Equation (4).

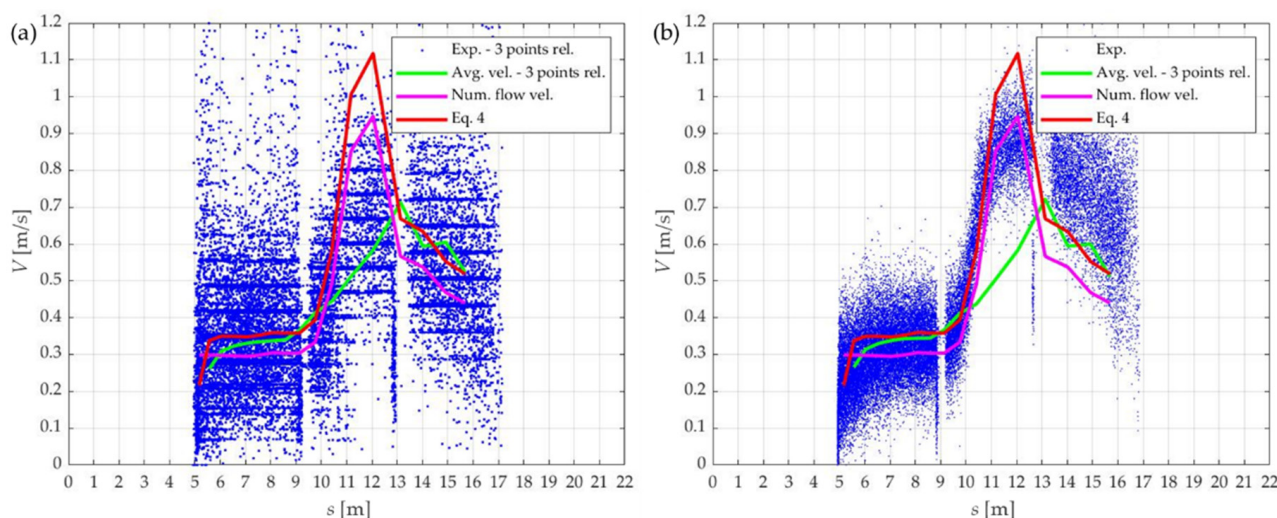


**Figure 4.** Comparison of the simulated flow velocity, the wood transport velocity (Equation (4)) and the sampled average experimental velocity for semi-congested wood transport simulation with (a) the experimental velocities of one test in semi-congested conditions (30 logs released at 3 points) and (b) the experimental velocities of an uncongested transport experiment [30].

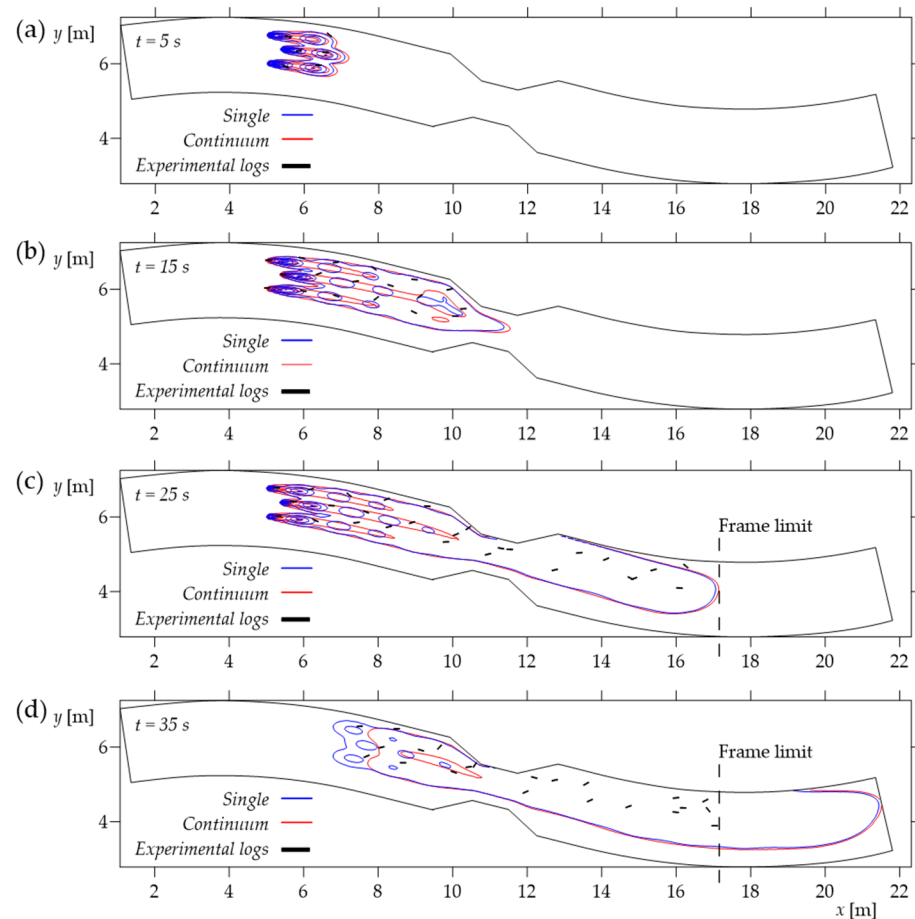
Since the cylinders enter the flow in different positions, they are subject to a variable velocity in the range of 0.07–1.2 m/s. In the upstream part of the flume, the velocity always remains below 0.8 m/s, with an average value around 0.35 m/s, then it increases and decreases due to the crossing of the narrowing. Empty parts of the graph are due to systematic acquisition issues due to field lighting but do not affect the analysis of data. The sampled average velocity follows the experimental trend. The flow velocity, computed by the numerical model, is generally higher, and even more is the transport velocity, which is modulated to replicate the surface velocity. The transport velocity is similar to the experimental average velocity up to  $s = 9$  m, then reaches a higher maximum of 1.1 m/s and returns closer to experimental values for  $s > 13$  m.

Figure 4b shows the experimental velocity of a realization of uncongested transport, in which cylinders were released one by one, avoiding any interaction, at a transversal distance equal to 0.4 m. This is one of the experiments used to derive the transport velocity expressed by Equation (4) [30]. The experimental velocities for uncongested transport are less dispersed than those of semi-congested experiments (Figure 4a) since, in this case, only one release point was employed. The transport velocity follows the experimental velocity up to  $s = 10$  m. Then, it presents higher values in the constriction and lower values when  $s > 13$  m. The simulated flow velocity is generally lower than the experimental one but reaches the same values in the constriction ( $s = 10$ – $12$  m), and the average experimental velocity, which refers to the semi-congested experiments in Figure 4a, is lower than the experimental trend in the narrowing and in the downstream part ( $s > 10$  m).

The differences highlighted between the experimental velocity for semi-congested conditions and the transport velocity computed by the model may certainly impact the matching of experimental and numerical results. However, since, at this stage, the aim is to test the existing model, the transport velocity is kept unchanged (Equation (4)).

### 3.2. Effect of the Release Conditions

In the Eulerian model, the different entertainment modes that may occur in real events are simulated for the three different release distances. For the *Single* and the *Continuum* modes, the results are compared with the experiments consisting of the release of a single log every 3 s (Figure 5, experiments with  $d_{tr} = (-40, 0, 40)$ ). Both methods catch the overall distribution of the cylinders, except for a few logs that are positioned out of the contour lines and the tendency of the numerical mass being slightly displaced towards the flume axis, while the experimental logs remain nearer to the left flume wall. The *Single* mode maintains a higher concentration (closed contour lines, with interval  $0.0005 \text{ m}^3/\text{m}^3$  for Figure 5) up to  $x = 8 \text{ m}$  as if each log was identifiable before its mass being distributed in the surrounding cells. In the *Continuum* mode, the concentration plumes are visible but do not identify single logs.



**Figure 5.** Top view of the flume comparing the experimental log positions and the contour maps for the *Single* and *Continuum* release modes, starting from (a–d) 5 s to 35 s, with a time step of 10 s.

Due to the different release methods, a slight variation in the localization of the wood concentration fronts is observed. The *Continuum* mode presents slightly advanced fronts (e.g., Figure 5b,d) since in that case, the mass is released in 27 s with an impulsive initial release at  $t = 0 \text{ s}$ , while for the *Single* mode the release is gradually distributed on a 3 s interval for each log.

Note that the geometric limit of the top-view recording is at about  $x = 17$  m, as shown by the dashed line in Figure 5. The trajectory of the logs that pass beyond the line is not available and, for this reason, no experimental log appears downstream of the dashed line.

To compare the results of the *Cumulative* release mode with the experiments, the position of all the experimental logs at a fixed time after each release is considered (Figure 6), as if they had all been released at the same time but neglected any interaction. In this way, the physical trajectory of each cylinder is disregarded, while the focus is on the probable distribution of the logs at a known time after their release.

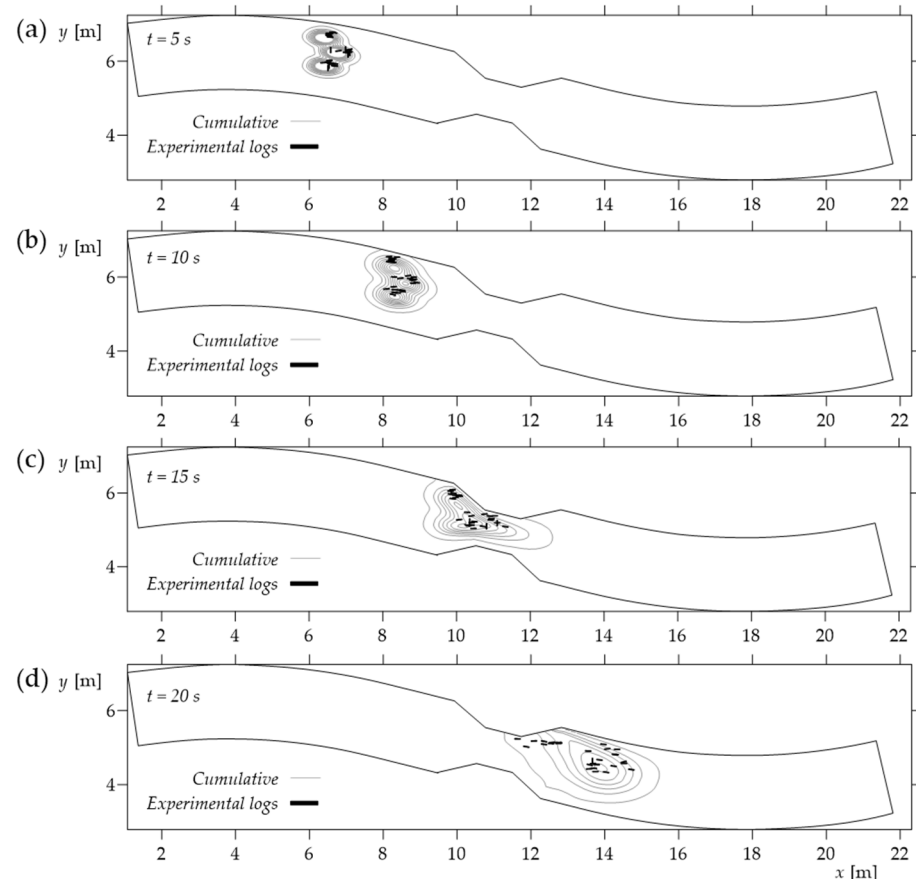


**Figure 6.** Top view of the flume—comparing the experimental log positions and the contour maps for the *Cumulative* release mode, starting from (a–d) 5 s to 20 s, with a time step of 5 s.

As shown by Figure 6, the peak of the numerical concentration follows the most probable position of the experimental logs, being able to model the delay of the fraction of the wood mass that flows nearer to the left bank (see in particular Figure 6c,d). Overall, the numerical wooden mass tends to spread towards the right side of the flume.

In Figure 6, the wood volume concentration limit is  $0.001 \text{ m}^3/\text{m}^3$ . The total transported mass in the channel reach, although varying in time with different patterns, is preserved by all the release modes, as shown in Figure 7, where it is compared with the total mass released in the channel.

### 3.3. Simulation Accuracy for the Single and Continuum Release Modes

To assess the model capacity in transporting surface wooden debris, ten target areas are identified in the flume from  $s = 4$  m to  $s = 16$  m (not to go beyond the downstream frame limit). The areas are contiguous, as shown in Figure 8a. Two areas (*a, f*) are upstream of the narrowing, two (*e, j*) are downstream of it. Six additional areas (*b, c, d, g, h, i*) are identified in the converging part, in the constriction and the diverging tract, and are limited by the flume walls and axis. To compare the experimental and the numerical results, the

experimental mass is obtained as the sum of the wooden mass of the logs that are located in the target area at each sampling time. Note that one log is accounted for if its mass center is included in the area. The numerical normalized mass is obtained as the sum of the wood mass in each cell included in the target area at the sampling time.

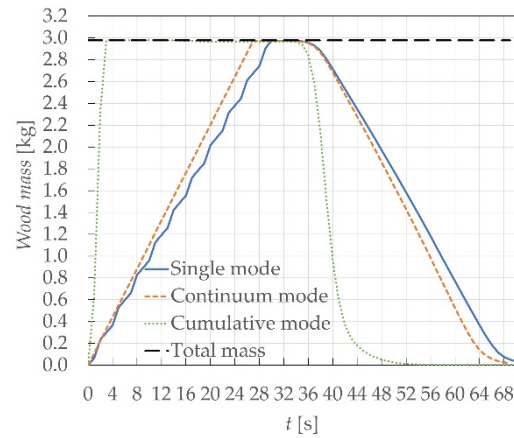


Figure 7. Diagram of the mass conservation along time for the three release modes.

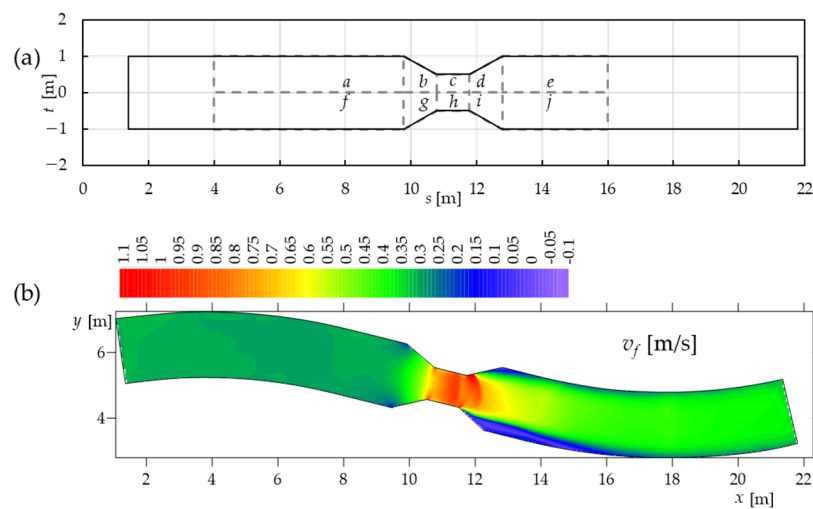
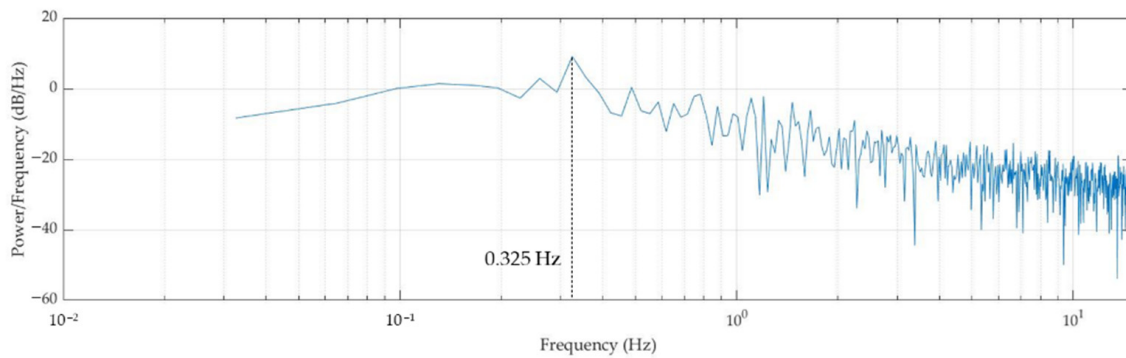


Figure 8. (a) Top view of the flume with target areas and (b) flow velocity contour map.

Both the experiments and the simulations are time discrete, i.e., the results are given at a specific time instant. To provide a significant comparison, the data must be sampled with an equal frequency. The sampling frequency was determined by analyzing the power/frequency spectrum (Figure 9) of the average experimental streamwise position for the tests with release distance  $d_{tr} = (-40, 0, 40)$ . As expected, the maximum frequency of 0.325 Hz corresponds to the release time interval of 3 s. According to the Shannon–Nyquist theorem, to avoid aliasing and information loss, the sampling period was set to 1.5 s, i.e., a frequency of 0.667 Hz, greater than twice the maximum frequency found through signal analysis. This sampling period was used both to sample the experimental results (the original data have a period of 0.0333 s, corresponding to the recording frame rate) and to write the output data for the numerical simulations. Note that this frequency does not affect the computational time step, defined in Section 2.2.



**Figure 9.** Power spectrum diagram with the selected sampling frequency.

Figures 10–12 compare the experimental and the numerical wood mass hydrographs in each target area, adopting either the *Single* release or the *Continuum* release mode, for the test series with release distance  $d_{tr} = (-20, 0, 20)$ ,  $d_{tr} = (-40, 0, 40)$ ,  $d_{tr} = (-60, 0, 60)$ , respectively. Each graph shows how the wood mass varies since the mass enters and exits the area. In all the areas, the mass increases, then it reaches a plateau when the input and output are in balance, and finally, it decreases when the input of mass ends. The mass in each area never reaches the maximum (about 2.97 kg, as shown in Figure 7) since it starts to flow out to the next area before the input ends. The total mass results are thus distributed in the different areas at different times. Note that the mass of one cylinder is about 0.099 kg.

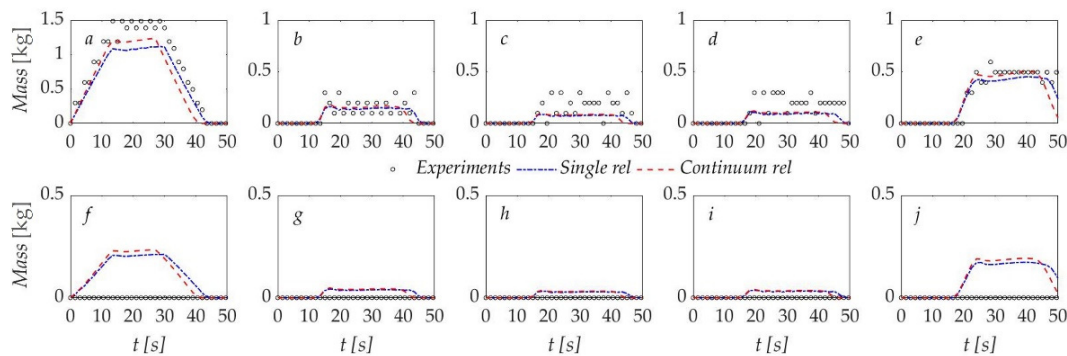


**Figure 10.** Wood mass in the target areas (letters a–j corresponds to the target areas in Figure 8a) for the experiments and the fully Eulerian simulations with  $d_{tr} = (-20, 0, 20)$ .

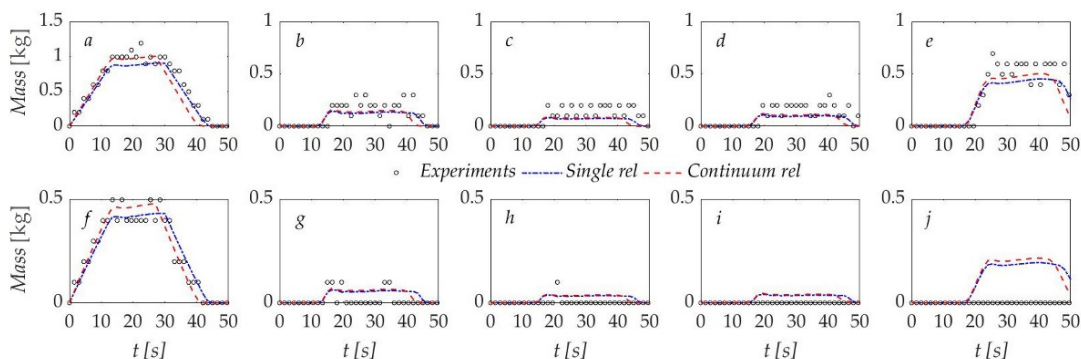


**Figure 11.** Wood mass in the target areas (letters a–j corresponds to the target areas in Figure 8a) for the experiments and the fully Eulerian simulations with  $d_{tr} = (-40, 0, 40)$ .

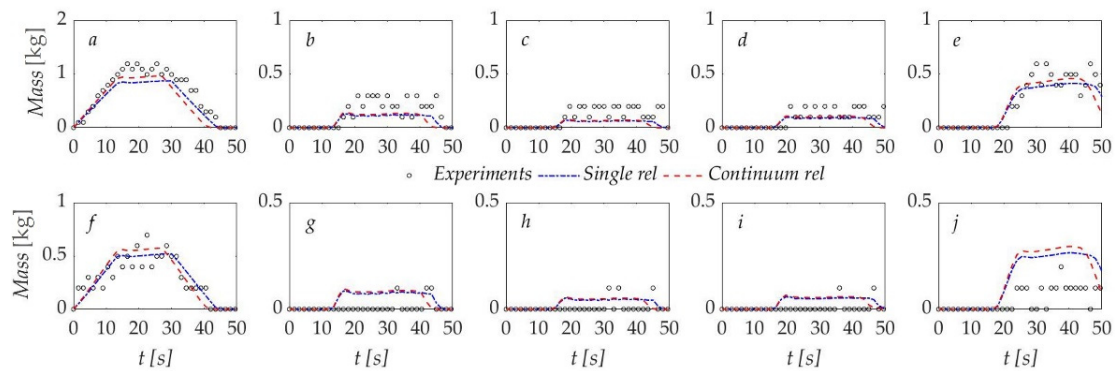


**Figure 12.** Wood mass in the target areas (letters *a–j* corresponds to the target areas in Figure 8a) for the experiments and the fully Eulerian simulations with  $d_{tr} = (-60, 0, 60)$ .

In Figure 10, the maximum experimental wood mass is observed in the left target areas (*a* to *e*), mainly due to the upstream curve that induces flow curvature and centrifugal acceleration, being nearly zero in the right target areas. The simulated wood mass is smoothly distributed in time and reaches lower values in the left areas and higher values in the right target areas. This reflects a higher diffusivity of the numerical result compared with the experiments, as the transported mass tends to spread also transversally towards the right flume wall. Forward and delayed tails of wood mass are observed for the numerical results along the time axis, especially in the downstream areas *c*, *d*, and *e*, while the experiments present sharper edges at the beginning and the end of the curves for any target areas.

In both Figures 11 and 12, compared to Figure 10, an increase in the experimental wood mass in the right target areas (*f* to *j*) is shown due to the larger distance among the release boxes that allows the logs to float below the flume axis. The numerical mass is similar to the experimental one in area *f*, while it is generally higher in the others, where random appearances of a few experimental logs are observed. An exception is area *j* for the largest release distance (Figure 12). In this case, several cylinders are observed, but the numerical mass remains higher. As in Figure 10, the numerical mass in the left areas is nearly the average or reaches at least the lower value of the experimental one. In any target area, the rising limb is replicated with a similar accuracy by the two release modes, while the decreasing limb is better simulated by the *Single* release mode.

Note that in the experiment logs are discrete quantities that transit through the target areas, while in the numerical model, the mass is a continuous quantity. In the first case, the experimental wood mass has been computed, accounting for the mass of the logs within the area (the mass of a log is included when its center of mass enters the target area). This results in a discontinuous trend of the mass. On the other hand, since the mass is a continuous quantity in the numerical model, it is more distributed over the sampling area despite the release mode.

To provide a quantitative comparison, the mean absolute error is computed for the experimental and numerical mass in each couple of target areas *a + f*, *b + g*, *c + h*, *d + i*, and *e + j* (Table 1). The largest errors appear in the initial or final target areas and are slightly higher for the *Continuum* release mode, which tends to anticipate the exit of the wood mass from the target area.

The actual wood mass transported by the modeled flow is computed as the sum of the wood mass in all the target areas at each time. As an example, in Table 2, the mass at  $t = 27$  s is shown for each target area.

By repeating the same procedure for all the sampling times, the total mass is obtained, as shown in Figure 13. At every time step, the total mass in the flume is lower than the total mass inserted (about 2.97 kg, Figure 7) because some logs exit the target areas before the end of the injection time, as also shown in Figure 5c. The experimental mass increases, then it reaches a maximum of 2.5–2.8 kg at  $t = 25.5$ – $28.5$  s depending on the initial release distance,

and then it decreases. Similar behavior is observed for the simulated mass. For the *Single* release mode, the increase is slightly delayed, and a plateau is observed at  $t = 25.5\text{--}30$  s. The decreasing limb is overlapped with the experimental one, except for  $d_{tr} = (-60, 0, 60)$  (Figure 13c), where it is slightly anticipated. For the *Continuum* release mode, the mass increase and the maximum level reached are very similar to the experimental ones, while the decreasing tract is anticipated. Considering the curves for the three release distances, the average correlation coefficient is 0.993 and 0.974 for the *Single* and *Continuum* release, respectively, while the average percentage error in estimating the maximum mass is 12.5% and 3.6%, respectively. This confirms that the *Single* mode better replicates the mass trend over time but underestimates the maximum value reached, i.e., the input and output of mass from each target area are not in time with the experiments.

**Table 1.** Mean absolute errors (MAE) for the experimental and numerical mass in each couple of target areas. Highlighted in italics are the highest values.

Release Distance	Release Mode	<i>a + f</i>	<i>b + g</i>	<i>c + h</i>	<i>d + i</i>	<i>e + j</i>
$d_{tr} = (-20, 0, 20)$	Single	0.076	0.043	0.059	0.063	<i>0.083</i>
	Continuum	0.113	0.046	0.061	0.065	<i>0.124</i>
$d_{tr} = (-40, 0, 40)$	Single	<i>0.079</i>	0.040	0.041	0.041	0.066
	Continuum	<i>0.116</i>	0.043	0.045	0.041	0.101
$d_{tr} = (-60, 0, 60)$	Single	<i>0.127</i>	0.056	0.050	0.039	0.094
	Continuum	<i>0.152</i>	0.064	0.052	0.045	0.142

**Table 2.** Mass at  $t = 27$  s for all the areas, for the experiments and simulations with  $d_{tr} = (-40, 0, 40)$ . The last column shows the total mass, as the sum of the values in each row.

	Mass at $t = 27$ s [kg]										Total Mass
	<i>a</i>	<i>b</i>	<i>c</i>	<i>d</i>	<i>e</i>	<i>f</i>	<i>g</i>	<i>h</i>	<i>i</i>	<i>j</i>	
Experiments	0.893	0.230	0.099	0.198	0.595	0.397	0	0	0	0	2.48
Single mode	0.903	0.125	0.06	0.095	0.408	0.430	0.053	0.032	0.036	0.181	2.33
Continuum mode	1.003	0.139	0.077	0.103	0.454	0.478	0.060	0.036	0.039	0.201	2.59

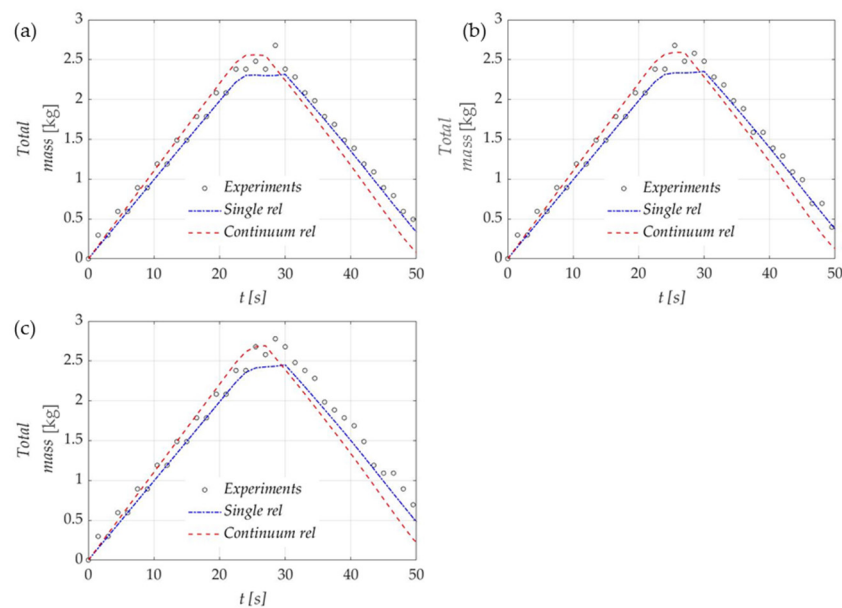


**Figure 13.** Total wood mass comprised in the black dashed line in Figure 8a for (a)  $d_{tr} = (-20, 0, 20)$ , (b)  $d_{tr} = (-40, 0, 40)$  and (c)  $d_{tr} = (-60, 0, 60)$ : fully Eulerian simulations vs. experiments.

### 3.4. Simulation Accuracy for the Cumulative Release Mode

The instantaneous release of the whole wood mass is performed to check the model capability to estimate the most probable positioning of large wood. In this case, the simulation should be regarded as a numerical test and not as the exact replication of the experiments since the release mode is different from the real one. The comparison is performed with the experimental data manipulated as the logs were released simultaneously, while during the experiments, a triplet of logs was released every 3 s.

For this reason, only one simulation is here shown, with the initial conditions set from the average conditions for release distance  $d_{tr} = (-40, 0, 40)$ . Figures 14 and 15 show the comparison of the wood mass variation in each target area and of the total mass in the flume. Focusing on the single areas, the experimental mass flows mainly in the left target areas, in the first right area with some logs also entering areas  $g$  and  $h$ . The numerical mass is evenly distributed and more diffused, as shown by the reduced peaks on the right side ( $b, c, d, e$ ) and the highest peaks on the left side ( $g, h, i, j$ ). The beginning and the end of the numerical mass trends are generally anticipated with respect to the experimental ones, suggesting that the transport velocity, together with the mass diffusion, could have fastened the front arrival in the target areas. The MAEs in Table 3, computed for each couple of target areas, reflect such inaccuracies in reproducing the mass evolution through the different target areas.

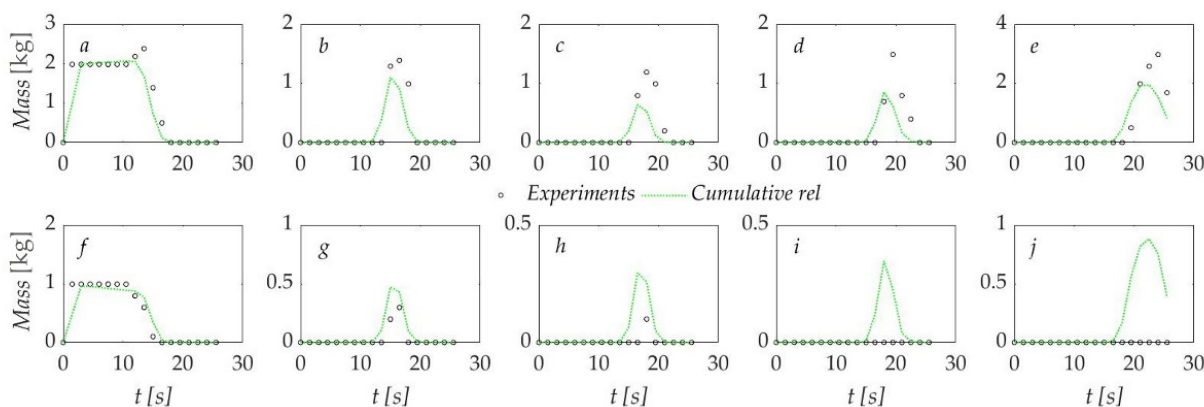


Figure 14. Wood mass in the target areas (letters  $a$ – $j$  corresponds to target areas in Figure 8a) for the experiments and fully Eulerian simulations with the cumulative release with  $d_{tr} = (-40, 0, 40)$ .

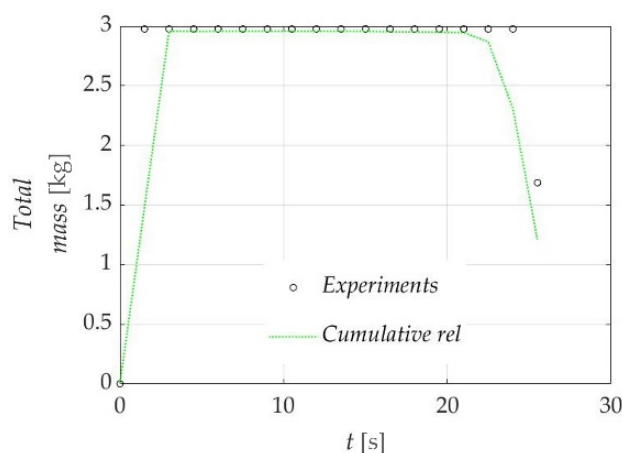


Figure 15. Total wood mass comprised in the black dashed line in Figure 8a for  $d_{tr} = (-40, 0, 40)$ : fully Eulerian simulations with cumulative release vs. experiments.

**Table 3.** Mean absolute errors (MAE) for the experimental and numerical mass in each couple of target areas. Highlighted in italics are the highest values.

Release Distance	Release Mode	<i>a + f</i>	<i>b + g</i>	<i>c + h</i>	<i>d + i</i>	<i>e + j</i>
$d_{tr} = (-40, 0, 40)$	Cumulative release	0.161	0.092	0.107	0.145	0.236

The total mass in the flume is obtained as the sum of the mass in each target area at each time (Figure 15). The numerical results present a little delay in the increasing tract since the entire mass is injected in 3 s. After 3 s, the numerical mass equals the total experimental mass flowing in the flume. The exit of the numerical mass is anticipated, probably because of the advanced position of the wood mass front in the simulation with respect to the foremost positions of logs in the experiments (as also shown in Figure 6). The correlation coefficient,  $R^2 = 0.891$ , confirms the mismatch observed, while the small percentage error in the estimate of the maximum mass,  $-1\%$ , demonstrates that the *Cumulative* mode is also able to reproduce the injected mass transport, despite some time lag.

#### 4. Discussion

The proposed model, which considers the transport of floating large wood as a passive substance, is applied to a series of flume experiments of semi-congested wood transport. To compare the experimental and numerical results and assess the model accuracy under steady flow with gradually varied velocity, the transported mass is compared in a series of target areas that are located along the flume. Different release distances and release modes are also tested.

The results show that the Eulerian numerical model tends to underestimate the wood mass in the left-side target areas (*a* to *e*) by distributing the wood mass also in the right-side areas. This is observed for any release distance and any release mode.

To assess if this depends on the proposed Eulerian model, a simulation of one test with  $d_{tr} = (-40, 0, 40)$  is also performed with the Eulerian–Lagrangian model ORSA2D\_WT to provide a comparison, as such models are considered as a benchmark in the literature when dealing with large wood transport.

The model, applied both to flume and field experiments [23,24], implements a dynamic subroutine to compute wood transport in the hydrodynamic model ORSA2D, i.e., the same hydrodynamic module used as the basis for the Eulerian model presented in the previous paragraphs. The hydrodynamic forces are computed for each cylinder with proper hydrodynamic coefficients [42]. A two-way coupling, i.e., the effect of the wood on the water, is also implemented. In this case, a single test, and not an average test, is simulated. Figure 16 shows a time sequence of the experimental and numerical log positions.

The initial positions for the numerical logs are derived from the experiments, as well as time-averaged planar and angular initial velocities. The numerical logs do not follow exactly the experimental log trajectories, but the log distribution and the time of arrival at the narrowing (Figure 16b) are similar. In the second part of the flume, the log position is more scattered and differs from the experiments. This can be ascribed to the increased turbulence and mixing in the divergent. Note that the hydrodynamic model does not include the modeling of turbulence, which contributes to the variation of log positions.

The mass variation in the target areas was also computed in this case, as shown in Figure 17. The Lagrangian model shows that a higher number of logs, with respect to the experiments, floats in the right-side target areas. The increase and decrease in mass in the left-side areas are well replicated. In this case, the MAE is always below 0.06 (0.042, 0.04, 0.045, 0.045 and 0.053 for areas *a + f*, *b + g*, *c + h*, *d + i* and *e + j*). The numerical total mass (Figure 18) follows the experimental one, both in terms of shape and maximum value. The correlation coefficient is 0.995, and the error for the maximum mass is zero. In this case, the impulsive increase in mass due to a single log entering the flume is visible both for the experiments and for the simulation, as the Lagrangian model treats each log as a separate entity.

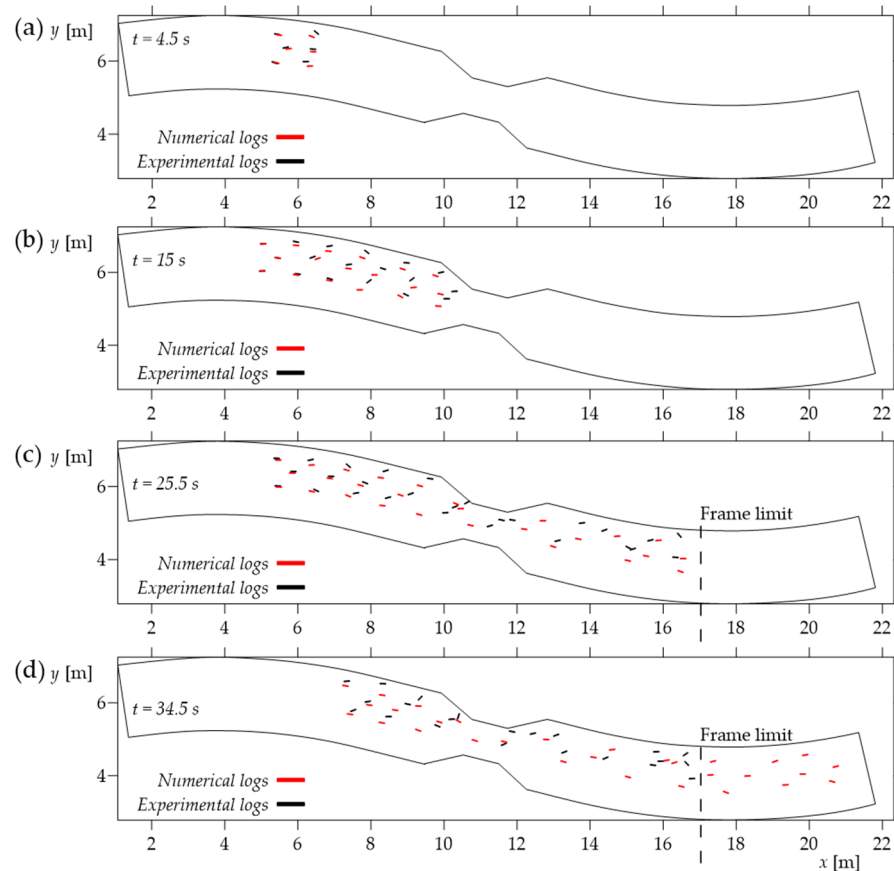


**Figure 16.** Top view of the flume comparing the experimental and numerical log positions from the Eulerian–Lagrangian simulation at different time instants: (a) 4.5 s, (b) 15 s, (c) 25.5 s and (d) 34.5 s.

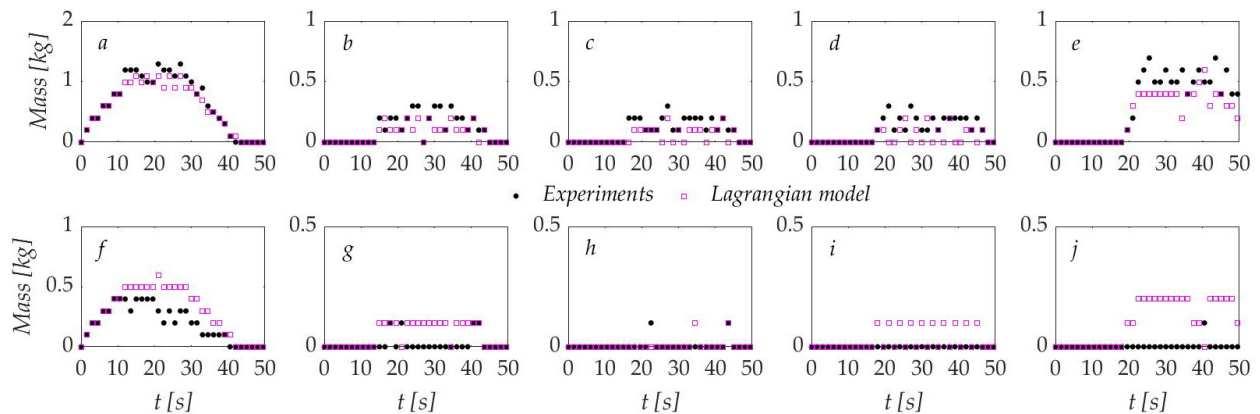


**Figure 17.** Wood mass in the target areas (letters a–j corresponds to target areas in Figure 8a) for the experiments and the Eulerian–Lagrangian simulations with  $d_{tr} = (-40, 0, 40)$ .

As the different mass distribution in the left and right side of the flume also appears in the Eulerian–Lagrangian model and seems to be independent of factors related to the test configuration, it may be related to differences in the simulated flow velocity that may affect the evaluation of the transport velocity in the Eulerian model and of the hydrodynamic forces in the Eulerian–Lagrangian approach. The comparison of the measured and simulated velocities (Figure 3) shows, indeed, some incongruity in terms of correlation, with values lower than 0.8, although the qualitative comparison of the velocity vectors (Figure 19) does not highlight major differences. The velocity magnitudes are consistent, as well as its direction, apart from two points of measure on the right side of the

flume, in the divergent and downstream of it, where the measured velocity appears to be much lower than the measured one, and two points on the left, in the divergent, where the numerical velocity is also lower than the measured one (about 0.6 m/s in the simulation, 0.89 m/s in the measurement, bordered by a dashed line in Figure 19). For the remaining points of measure, the velocity vectors are in agreement, with a correlation coefficient  $R^2 = 0.947$  (against a value of 0.762 obtained considering the entire set), confirming the overall reliability of the hydrodynamic model, apart from local uncertainties. The higher velocity on the right side of the flume and the lower one on the left may contribute to the displacement of the numerical wood mass across the flume axis.

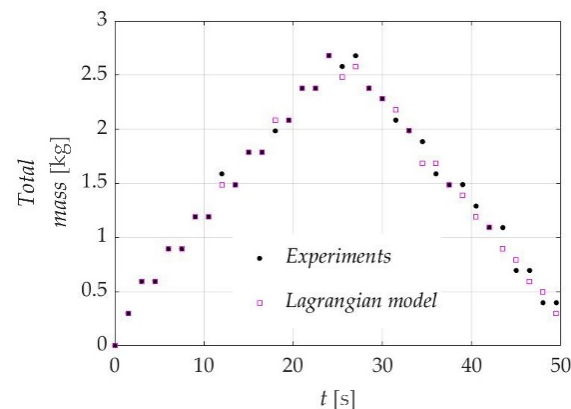


**Figure 18.** Total wood mass comprised in the black dashed line in Figure 8a for  $d_{tr} = (-40, 0, 40)$ : Eulerian–Lagrangian simulations vs. experiments.

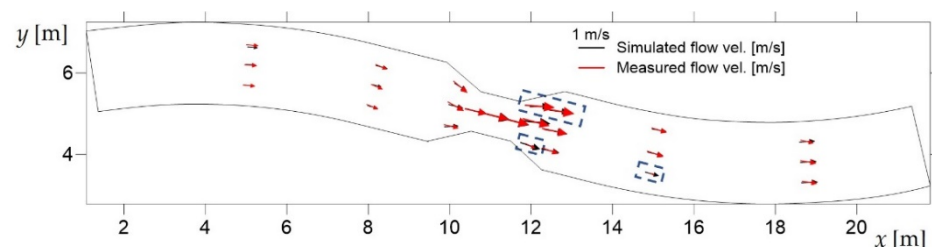


**Figure 19.** Comparison of the measured and simulated velocity vectors. The vectors with the largest difference between measurements and simulation are bordered by a dashed line.

Considering the mass variation along the flume axis, the model accuracy is not uniform along with the considered target areas, with the highest differences recorded in the initial or final areas and for the *Cumulative* release mode. The main differences can be ascribed both to the different distribution of the mass across the flume axis and to the different timing of increase and decrease in the mass in each target area. This is also observed when considering the mass variation in the entire flume. The *Continuum* mode tends to anticipate the mass reduction, although it can simulate with higher accuracy the wood mass peak with respect to the *Single* release mode. For the *Cumulative* release mode, too, the maximum mass is well-replicated while both the rising and decreasing limbs of the curve are different from the experimental trend.

The release distance does not affect the model accuracy, and the calculated errors are similar for any test configuration.

By comparing the results of the fully Eulerian model and the Eulerian–Lagrangian model, it appears that the mass distribution in the target areas is similar, although the computed errors are generally lower for the latter. In addition, the Eulerian–Lagrangian model can replicate the increase and decrease in the total mass by maintaining its discontinuous trend, which is typical of the transport of discrete elements.

## 5. Conclusions

The analysis of the errors resulting from the different release modes shows that the *Single* release mode provides better temporal evolution of the mass, while the *Continuum* and the *Cumulative* release modes replicate with higher accuracy the maximum mass in the flume. A tendency to transport the mass across the flume axis (from the left side to the right side) is shown by all the release modes, leading to the reduction of the accuracy when considering single target areas.

The overall accuracy is, however, lower than the accuracy of the Eulerian–Lagrangian model, which shows similar issues regarding the distribution of the cylinders in the right and left sides of the flume.

The experimental campaign aimed at modeling semi-congested transport conditions, in which the interactions between logs were low and observed only downstream of the constriction. Under such conditions, the cylinders float separately and maintain a scattered distribution for most of the time. Such behavior is better replicated by the Lagrangian approach, which considers each cylinder as a single entity transported by the flow.

The application of the fully Eulerian model shows that considering the wood mass as a superficial substance transported by the flow affects the result accuracy, especially when the interaction between the transported cylinders is low. However, although under the highlighted limitations, the transport of large wood modeled with a fully Eulerian approach provides promising results since it may help in overcoming some issues of the Eulerian–Lagrangian approach. For example, when dealing with the gradual entrainment of wood, detailed information on the exact timing of the entrainment of a single log is not necessary. The estimate, or the design of different scenarios, of the total mass and the total entrainment time, in addition to the entrainment location, are sufficient to perform the simulations, reducing the amount of required input data. Considering its highest accuracy in replicating the total mass, the *Continuum* mode should be preferred, probably smoothing the rising and decreasing limb to improve the modeling of the mass variation.

As shown by the simulation with the *Cumulative* release mode, the Eulerian model could also be employed to estimate the most probable position of floating large wood mass, taking care, again, of the slight acceleration of the increase and decrease in wood mass.

The time lags observed within the fully Eulerian model can depend on the transport velocity. The analysis of the experimental velocities shows that a higher difference exists between the experimental velocity for semi-congested transport and the Eulerian model transport velocity, based on uncongested transport data. To overcome this issue, which may affect the mass variation in the single target areas and in the flume, a re-modulation of the transport velocity should take into consideration the effect of the semi-congested transport on the flow velocity. This may be obtained by implementing a two-way coupling between the flow velocity and the transported mass for the Eulerian model, thus considering the interaction between the wood and the flow and abandoning the strict definition of large wood as a passive substance.

In addition to the ability to model wood passage at critical sections, the fundamental steps towards the complete applicability of the model are (i) the simulation of jam formation, including the arrest mechanism, and (ii) the two-way coupling between shallow water and wood transport equations to allow the model to predict not only the influence of wood on the water but also the backwater effect in case of jam formation. As to the author's knowledge, such features are provided by some Lagrangian models dealing with large wood transport, but additional research, including experiments and mathematical conceptualizations, are needed to extend these capacities to the Eulerian approach.

**Author Contributions:** Conceptualization, E.P., A.A., S.S., G.P. and S.M.; methodology, E.P., A.A., S.S., G.P. and S.M.; software, E.P., G.P. and S.S.; validation, E.P.; formal analysis, E.P. and S.M.; investigation, E.P. and S.M.; resources, G.P. and E.P.; data curation, E.P.; writing—original draft preparation, E.P. and S.M.; writing—review and editing, E.P., S.M., G.P., S.S. and A.A.; visualization, E.P.; supervision, A.A., S.S. and G.P.; project administration, G.P.; funding acquisition, G.P. All authors have read and agreed to the published version of the manuscript.

**Funding:** This research was funded by: CE4WE (Circular Economy for Water and Energy) founded by Regione Lombardia, POR FESR 2014-2020 ASSE I—CUP E18I20000020007, ID 1139857; the Flood Risk Management Policies (FLORIMAP) project, which has been supported by Fondazione Cariplo, grant n° 2017/0708; the project STEEP STREAMS financed under the ERA-NET Cofund WaterWorks2014 Call, an integral part of the 2015 Joint Activities developed by the Water Challenges for a Changing World Joint Programme Initiative (Water JPI).

**Data Availability Statement:** Data are available upon request by email to the corresponding author.

**Acknowledgments:** The authors thank Francesca Taschini and the staff of DICAM at the University of Trento for performing the experimental campaign and Andrea Fenocchi for the suggestions for data analysis. We are grateful to three anonymous reviewers who helped improve the paper.

**Conflicts of Interest:** The authors declare no conflict of interest.

## References

1. Comiti, F.; Lucía, A.; Rickenmann, D. Large wood recruitment and transport during large floods: A review. *Geomorphology* **2016**, *269*, 23–39. [[CrossRef](#)]
2. Kramer, N.; Wohl, E. Rules of the road: A qualitative and quantitative synthesis of large wood transport through drainage networks. *Geomorphology* **2017**, *279*, 74–97. [[CrossRef](#)]
3. Ruiz-Villanueva, V.; Bodoque, J.M.; Díez-Herrero, A.; Bladé, E. Large wood transport as significant influence on flood risk in a mountain village. *Nat. Hazards* **2014**, *74*, 967–987. [[CrossRef](#)]
4. Kimura, N.; Tai, A.; Hashimoto, A. Flood caused by driftwood accumulation at a bridge. *Int. J. Disaster Resil. Built Environ.* **2017**, *8*, 466–477. [[CrossRef](#)]
5. SABO Division. *Guideline for Driftwood Countermeasures (Proposal and Design)*; SABO Division: Tokyo, Japan, 2000.
6. Schweizerisches Talsperrenkomitee; Comité Suisse des Barrages; Comitato Svizzero delle Dighe; Swiss Committee on Dams. Floating Debris at Reservoir Dam Spillways. 2017. Available online: [http://www.swissdams.ch/en/publications/publications-csb/2017\\_Floatingdebris.pdf](http://www.swissdams.ch/en/publications/publications-csb/2017_Floatingdebris.pdf) (accessed on 10 January 2022).
7. Dihel, T.H. *Potential Drift Accumulation at Bridges*; USA Department of Transportation: Washington, DC, USA; USA Federal Highway Administration, Research and Development: Washington, DC, USA; Turner-Fairbank Highway Research Center: McLean, VA, USA, 1997.
8. Schmocker, L.; Weitbrecht, V. Driftwood: Risk Analysis and Engineering Measures. *J. Hydraul. Eng.* **2013**, *139*, 683–695. [[CrossRef](#)]
9. Wohl, E.; Bledsoe, B.P.; Fausch, K.D.; Kramer, N.; Bestgen, K.R.; Gooseff, M.N. Management of Large Wood in Streams: An Overview and Proposed Framework for Hazard Evaluation. *JAWRA J. Am. Water Resour. Assoc.* **2016**, *52*, 315–335. [[CrossRef](#)]
10. Bradley, J.B.; Richards, D.L.; Bahner, C.D. *Debris Control Structures—Evaluation and Countermeasures: Hydraulic Engineering Circular 9*; USA Federal Highway Administration: Washington, DC, USA, 2005.
11. Panici, D.; Kripakaran, P. Trapping Large Wood Debris in Rivers: Experimental Study of Novel Debris Retention System. *J. Hydraul. Eng.* **2021**, *147*, 04020101. [[CrossRef](#)]
12. Lyn, D.A.; Cooper, T.; Yi, Y.-K.; Sinha, R.; Rao, A.R. *Debris Accumulation at Bridge Crossings: Laboratory and Field Studies*; Indiana Department of Transportation and Purdue University: West Lafayette, IN, USA, 2003.
13. Schalko, I.; Schmocker, L.; Weitbrecht, V.; Boes, R.M. Risk reduction measures of large wood accumulations at bridges. *Environ. Fluid Mech.* **2020**, *20*, 485–502. [[CrossRef](#)]
14. Schmocker, L.; Hager, W.H. Scale Modeling of Wooden Debris Accumulation at a Debris Rack. *J. Hydraul. Eng.* **2013**, *139*, 827–836. [[CrossRef](#)]
15. Meninno, S.; Canelas, R.B.; Cardoso, A.H. Coupling check dams with large wood retention structures in clean water. *Environ. Fluid Mech.* **2020**, *20*, 619–634. [[CrossRef](#)]
16. Rossi, G.; Armanini, A. Experimental analysis of open check dams and protection bars against debris flows and driftwood. *Environ. Fluid Mech.* **2020**, *20*, 559–578. [[CrossRef](#)]
17. Schalko, I. Wood retention at inclined racks: Effects on flow and local bedload processes. *Earth Surf. Process. Landf.* **2020**, *45*, 2036–2047. [[CrossRef](#)]
18. Furukawa, M.; Tsutsumi, D.; Muto, H.; Uchida, T.; Suzuki, T.; Horiguchi, T. Flume Experiments Evaluating the Efficacy of a Large Wood Trap Featuring Horizontal Rods. *Water* **2021**, *13*, 1837. [[CrossRef](#)]
19. Yang, J. *Experiences from Hydraulic Model Tests in Dam Rebuilding Projects*; Energiforsk: Stockholm, Sweden, 2010.
20. Simonett, S.; Detert, M.; Weitbrecht, V. Driftwood Retention to Minimize Flood Risk for the City of Zurich—Physical Experiments. In Proceedings of the 12th Congress INTERPRAEVENT 2012—Grenoble/France, Grenoble, France, 23–26 April 2012; pp. 803–810.
21. Ruiz-Villanueva, V.; Bladé, E.; Sánchez-Juny, M.; Martí-Cardona, B.; Díez-Herrero, A.; Bodoque, J.M. Two-dimensional numerical modeling of wood transport. *J. Hydroinform.* **2014**, *16*, 1077–1096. [[CrossRef](#)]
22. Stockstill, R.L.; Daly, S.F.; Hopkins, M.A. Modeling Floating Objects at River Structures. *J. Hydraul. Eng.* **2009**, *135*, 403–414. [[CrossRef](#)]

23. Persi, E.; Petaccia, G.; Sibilla, S.; Brufau, P.; García-Navarro, P. Calibration of a dynamic Eulerian-lagrangian model for the computation of wood cylinders transport in shallowwater flow. *J. Hydroinform.* **2019**, *21*, 164–179. [[CrossRef](#)]
24. Persi, E.; Petaccia, G.; Sibilla, S.; Lucía, A.; Andreoli, A.; Comiti, F. Numerical modelling of uncongested wood transport in the Rienz river. *Environ. Fluid Mech.* **2020**, *20*, 539–558. [[CrossRef](#)]
25. Kimura, I.; Kang, T.; Kato, K. 3D-3D Computations on Submerged-Driftwood Motions in Water Flows with Large Wood Density around Driftwood Capture Facility. *Water* **2021**, *13*, 1406. [[CrossRef](#)]
26. Okamoto, T.; Tanaka, K.; Matsumoto, K.; Someya, T. Influence of velocity field on driftwood accumulation at a bridge with a single pier. *Environ. Fluid Mech.* **2021**, *21*, 693–711. [[CrossRef](#)]
27. Braudrick, C.A.; Grant, G.E.; Ishikawa, Y.; Ikeda, H. Dynamics of Wood Transport in Streams: A Flume Experiment. *Earth Surf. Process. Landf.* **1997**, *22*, 669–683. [[CrossRef](#)]
28. Piton, G.; Horiguchi, T.; Marchal, L.; Lambert, S. Open check dams and large wood: Head losses and release conditions. *Nat. Hazards Earth Syst. Sci.* **2020**, *20*, 3293–3314. [[CrossRef](#)]
29. Meninno, S.; Persi, E.; Petaccia, G.; Sibilla, S.; Armanini, A. An experimental and theoretical analysis of floating wood diffusion coefficients. *Environ. Fluid Mech.* **2020**, *20*, 593–617. [[CrossRef](#)]
30. Persi, E.; Petaccia, G.; Sibilla, S.; Bentivoglio, R.; Armanini, A. A one-way coupled hydrodynamic advection-diffusion model to simulate congested large wood transport. *Hydrology* **2021**, *8*, 21. [[CrossRef](#)]
31. Steeb, N.; Rickenmann, D.; Badoux, A.; Rickli, C.; Waldner, P. Large wood recruitment processes and transported volumes in Swiss mountain streams during the extreme flood of August 2005. *Geomorphology* **2017**, *279*, 112–127. [[CrossRef](#)]
32. Tonon, A.; Picco, L.; Rainato, R. Test of methodology for developing a large wood budget: A 1-year example from a regulated gravel bed river following ordinary floods. *CATENA* **2018**, *165*, 115–124. [[CrossRef](#)]
33. Schenk, E.R.; Moulin, B.; Hupp, C.R.; Richter, J.M. Large wood budget and transport dynamics on a large river using radio telemetry. *Earth Surf. Process. Landforms* **2014**, *39*, 487–498. [[CrossRef](#)]
34. Schalko, I.; Schmocker, L.; Weitbrecht, V.; Boes, R.M. Laboratory study on wood accumulation probability at bridge piers. *J. Hydraul. Res.* **2020**, *58*, 566–581. [[CrossRef](#)]
35. Piton, G.; Recking, A. Design of Sediment Traps with Open Check Dams. I: Hydraulic and Deposition Processes. *J. Hydraul. Eng.* **2016**, *142*, 04015045. [[CrossRef](#)]
36. Furlan, P.; Pfister, M.; Matos, J.; Amado, C.; Schleiss, A.J. Blockage Probability Modeling of Large Wood at Reservoir Spillways With Piers. *Water Resour. Res.* **2021**, *57*, e2021WR029722. [[CrossRef](#)]
37. Petaccia, G.; Natale, L. 1935 Sella Zerbino Dam-Break Case Revisited: A New Hydrologic and Hydraulic Analysis. *J. Hydraul. Eng.* **2020**, *146*, 05020005. [[CrossRef](#)]
38. Fenocchi, A.; Petaccia, G.; Sibilla, S. Modelling flows in shallow (fluvial) lakes with prevailing circulations in the horizontal plane: Limits of 2D compared to 3D models. *J. Hydroinform.* **2016**, *18*, 928–945. [[CrossRef](#)]
39. Murillo, J.; Burguete, J.; Brufau, P.; García-Navarro, P. Coupling between shallow water and solute flow equations: Analysis and management of source terms in 2D. *Int. J. Numer. Methods Fluids* **2005**, *49*, 267–299. [[CrossRef](#)]
40. Morales-Hernández, M.; Murillo, J.; García-Navarro, P. Diffusion-dispersion numerical discretization for solute transport in 2D transient shallow flows. *Environ. Fluid Mech.* **2019**, *19*, 1217–1234. [[CrossRef](#)]
41. MacVicar, B.; Piégay, H. Implementation and validation of video monitoring for wood budgeting in a wandering piedmont river, the Ain River (France). *Earth Surf. Process. Landf.* **2012**, *37*, 1272–1289. [[CrossRef](#)]
42. Persi, E.; Petaccia, G.; Fenocchi, A.; Manenti, S.; Ghilardi, P.; Sibilla, S. Hydrodynamic coefficients of yawed cylinders in open-channel flow. *Flow Meas. Instrum.* **2019**, *65*, 288–296. [[CrossRef](#)]